

Robust retrieval of material chemical states in X-ray microspectroscopy

Ting Wang, Xiaotong Wu, Jizhou Li, Chao Wang

Abstract—X-ray microspectroscopic techniques are essential for studying morphological and chemical changes in materials, providing high-resolution structural and spectroscopic information. However, its practical data analysis for reliably retrieving the chemical states remains a major obstacle to accelerating the fundamental understanding of materials in many research fields. In this work, we propose a novel data formulation model for X-ray microspectroscopy and develop a dedicated unmixing framework to solve this problem, which is robust to noise and spectral variability. Moreover, this framework is not limited to the analysis of two-state material chemistry, making it an effective alternative to conventional and widely-used methods. In addition, an alternative directional multiplier method with provable convergence is applied to obtain the solution efficiently. Our framework can accurately identify and characterize chemical states in complex and heterogeneous samples, even under challenging conditions such as low signal-to-noise ratios and overlapping spectral features. Extensive experimental results on simulated and real datasets demonstrate its effectiveness and reliability.

Index Terms—X-ray microspectroscopy; image unmixing; total variation; Plug-and-Play prior.

I. INTRODUCTION

X-RAY absorption spectroscopy (XAS) is a scientific technique that utilizes X-rays to investigate the electronic and structural properties of materials. However, the spatial resolution of XAS is typically limited to the micron or sub-micron scale, which poses a challenge when studying materials with complex or heterogeneous structures. In recent years, spectroscopic full-field transmission X-ray microscopy (TXM) has emerged as a novel tool for nanoscale chemical imaging, with great potential in various multidisciplinary fields [1, 2]. By imaging at energy points across the absorption edge of the element of interest, TXM offers both high spatial resolution and chemical-specific information. Sub-50-nm resolution X-ray absorption near-edge structure (XANES) spectroscopy is routinely achieved with TXM-XANES, mainly operating in the hard X-ray regime (5 to 12 keV) [3–5]. Its application areas include materials science, physics, chemistry, and biology. For instance, it can be used for chemical mapping in battery studies [6, 7] and mesoscale degradation [8].

Ting Wang, Xiaotong Wu, and Chao Wang are with the Department of Statistics and Data Science, Southern University of Science and Technology, Shenzhen 518055, China. Chao Wang is also with National Centre for Applied Mathematics Shenzhen, Shenzhen 518055, China.

Jizhou Li is with the School of Data Science, City University of Hong Kong, Kowloon, Hong Kong.

Chao Wang was partially supported by the Natural Science Foundation of China (No. 12201286), HKRGC Grant No. CityU11301120, and the Shenzhen Fundamental Research Program JCYJ20220818100602005. (Corresponding author: Chao Wang, email: wangc6@sustech.edu.cn)

In TXM-XANES, the intensity change of each pixel is scrutinized to generate XANES spectra that are matched against reference compounds. Some common techniques, including the edge-50 or linear combination fitting (LCF) [1], are used to fit the spectra, then a two-dimensional colormap is constructed to display the chemical phase combination of each pixel. The XANES edge-50 point (energy at 0.5 spectrum position), which measures the absorption spectra of materials within the energy range of 5 keV to 12 keV, is a specific type of XANES spectrometer. The utilization of the edge-50 XANES technique has been progressively examined for characterizing the chemical composition and structure of environmental material [9]. On the other hand, [10] proposed using LCF to determine the phase composition of a chemical sample from normalized XANES spectra. The XANES image at each pixel represents a spectrum at a particular location, which can be fitted with reference spectra to produce spatially resolved chemical state information. This technique significantly simplifies the processing and analysis of XANES spectra using LCF. These traditional methods have been extensively used in the literature [11–13].

Although traditional methods are widely applicable, these rely on the high quality of XANES imaging. In this case, a relatively slow acquisition process, with the recording of hundreds or thousands of energy points, is needed to achieve sufficient energy resolution. Fast TXM-XANES imaging is crucial for reliably solving morphological chemical phase transitions, as in 3D battery material research. To increase the speed of TXM-XANES imaging, energy points are reduced, or X-ray exposure time is minimized, which is more favorable for radiation-sensitive samples, similar to low-dose medical X-ray imaging applications. However, excessively short exposure times can result in measurements with strong noise [14]. Furthermore, during the process of acquiring XANES data, there are many variations in the X-ray exposure conditions, and inherent material properties, which contribute to the variability of XANES spectra [15]. In the face of strong noise and spectral variability, the edge-50 and LCF methods fail to obtain a reasonable interpretation of elemental and chemical information. Despite efforts to optimize microscope hardware, the physical limitations of the TXM imaging system remain difficult to overcome. To address this obstacle, computational algorithm development is inevitable for improving downstream analysis through fitting results.

Spectral unmixing methods [16] have numerous applications in image science, including remote sensing [17–19], optical microscopy [20], and X-ray imaging [21–23]. The unmixing technique aims to decompose a spectrum of mixed pixels into

a set of distinct spectral signatures, known as endmembers, along with their corresponding fractional abundances [24, 25]. By utilizing spectral unmixing in X-ray microspectroscopy, the chemical states of materials can be directly obtained bypassing the fitting process. Various regularizations have been developed in spectral unmixing methods to utilize the prior information on the abundance map against noise. In addition, in the face of spectral variability, many model formulations have been proposed in the unmixing problems [26–30]. The principle underlying the LCF method is essentially spectral unmixing [16], whereby the mixture is analyzed by determining the contribution of the reference spectra. However, it is sensitive to noise and limited in handling problems with spectral variability.

The XANES unmixing task involving spectral variability can be formulated as an optimization model with some proper priors. We employ two regularization techniques to achieve this: the total-variation (TV) regularizer and the Plug-and-Play (PnP) prior. The TV regularizer is applied to the reconstructed image to incorporate spatial and spectral information through pixel connections in the unmixing process [31, 32]. On the other hand, the PnP technique utilizes state-of-the-art denoisers to tackle linear inverse problems in various hyperspectral image processing tasks [33–37]. The main contributions of this paper are summarized as follows:

- We present a novel and robust framework for X-ray XANES imaging, which incorporates various realistic factors that affect the spectra, such as noise and spectral variability.
- The convergence of our proposed framework with TV regularization is theoretically analyzed, demonstrating its effectiveness and applicability.
- Our proposed framework is evaluated extensively using both quantitative and qualitative methods on synthetic and real datasets. The results indicate that our proposed methods surpass the state-of-the-art. Especially our framework with a PnP prior achieves the best performance.

The rest of the paper is organized as follows. Section II briefly describes two related works. In Section III, we propose a novel data formulation model for the material chemical states retrieval in X-ray microspectroscopy and the corresponding algorithms to solve it. The convergence analysis is shown in Section IV. Section V presents the experimental results and some subsequent discussions. Finally, Section VI provides a summary and future perspectives.

II. RELATED WORK

This section will present a concise overview of two conventional methods to address this problem. Furthermore, the form of the edge-50 and LCF serves as the baseline for our proposed approach.

A. Edge-50

The edge-50 point, representing the energy at the 0.5 spectrum position, is a crucial parameter in studying chemical state changes during battery cycling. It is often used to determine the phase map in a TXM-XANES system [38, 39].

After preprocessing and the post-edge and pre-edge region normalization [1] of XANES images, a XANES spectrum is constructed for each pixel by plotting normalized absorption versus energy. We can then obtain the ratio of chemical materials for each pixel by comparing the energies at the 0.5 spectrum position from the referenced spectra.

B. Linear combination fitting (LCF)

Besides the edge-50, LCF is another technique used to extract information about the electronic structure of elements in a complex sample from XANES spectra [10]. By using a least-squares approach, this technique decomposes the spectrum into a linear combination of reference spectra from known compounds. In fact, LCF is the classical linear mixing model (LMM) in the hyperspectral imaging unmixing field [16, 26].

Here the observed XANES image is represented by $\mathbf{Y} = [\mathbf{y}_1, \mathbf{y}_2, \dots, \mathbf{y}_N] \in \mathbb{R}^{T \times N}$, where each column vector is obtained by lexicographically ordering the TXM image with size $N = M \times K$, and T is the number of energy points. The LCF model generates the noisy measurements \mathbf{Y} from the chemical phase map $\mathbf{X} = [\mathbf{x}_1, \mathbf{x}_2, \dots, \mathbf{x}_n] \in \mathbb{R}^{L \times N}$, pixel-wisely.

$$\mathbf{y}_k = \mathbf{A}\mathbf{x}_k + \mathbf{r}_k, \quad k = 1, \dots, N, \quad (1)$$

where $\mathbf{A} \in \mathbb{R}^{T \times L}$ is the dictionary, representing the reference materials spectra in the XANES images, L is the number of materials, and \mathbf{r}_k is assumed to follow Gaussian distribution. In other words, (1) can be rewritten in a matrix form:

$$\mathbf{Y} = \mathbf{A}\mathbf{X} + \mathbf{R}, \quad (2)$$

by considering all the pixels. Since the weight of a linear combination or chemical phase map is non-negative and sum-to-one, the estimation of the chemical phase map can be obtained by solving the following optimization problem:

$$\begin{aligned} \min_{\mathbf{X}} \quad & \frac{1}{2} \|\mathbf{Y} - \mathbf{A}\mathbf{X}\|_F^2 \\ \text{s.t.} \quad & \mathbf{X} \geq \mathbf{0}, \quad \mathbf{1}^T \mathbf{X} = \mathbf{1}. \end{aligned} \quad (3)$$

The chemical phase map \mathbf{X} in a model (3) can be obtained using a non-negative constrained least squares algorithm, such as [40].

Although traditional methods can quickly determine the composition of unknown samples, these methods are not robust under strong noise settings.

III. PROPOSED ROBUST UNMIXING FRAMEWORK

This section presents two models for effectively unmixing XANES images from model-based and learning-based perspectives, respectively. Both of them are solved by ADMM-based algorithm.

A. Model formulation

The spectral variability induced by the various conditions can be effectively modeled by approximating the dictionary matrix of each pixel with the scaled version of the reference

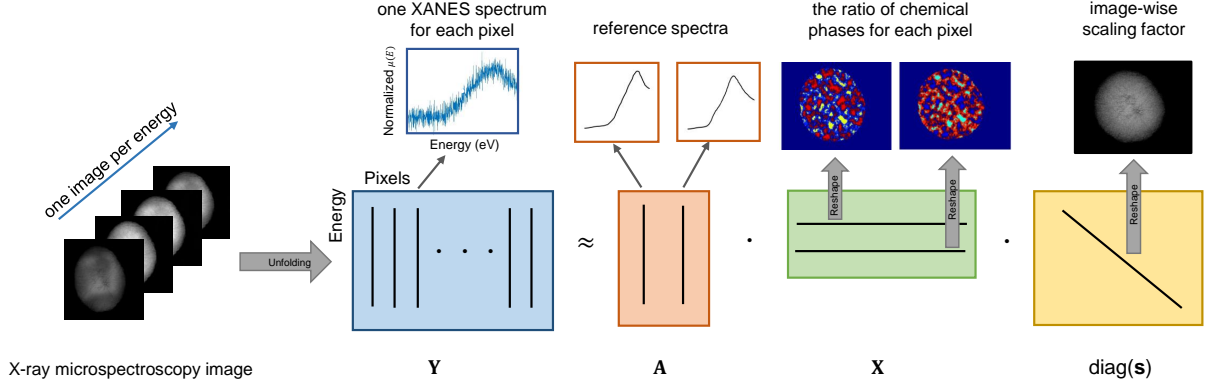


Fig. 1. Framework of the proposed model for material chemical states retrieval in the form of unmixing for X-ray microspectroscopy. The normalized XANES spectra from each pixel are unmixing to create a chemical phase map \mathbf{X} , which also takes into account the scaling factor on the image.

spectra. We propose an extended LCF model by considering the variability in each pixel, i.e., (1) can be changed to

$$\mathbf{y}_k = s_k \mathbf{A} \mathbf{x}_k + \mathbf{r}_k, \quad k = 1, \dots, N, \quad (4)$$

where s_k is a scalar in the k -th pixel. Similar to (2), we get the matrix form of (4) as

$$\mathbf{Y} = \mathbf{A} \mathbf{X} \text{diag}(\mathbf{s}) + \mathbf{R}, \quad (5)$$

where $\text{diag}(\mathbf{s})$ represents a diagonal matrix with its diagonal values $\mathbf{s} = [s_1, s_2, \dots, s_N]^T$ and $s_i \geq 0, \forall i \in 1, \dots, N$. Fig. 1 gives the macro diagram of spectral unmixing for the XANES imaging. With (5), we get an optimization problem:

$$\begin{aligned} \min_{\mathbf{X}, \mathbf{s}} \quad & \frac{1}{2} \|\mathbf{Y} - \mathbf{A} \mathbf{X} \text{diag}(\mathbf{s})\|_F^2 \\ \text{s.t.} \quad & \mathbf{X} \geq \mathbf{0}, \mathbf{s} \geq \mathbf{0}, \mathbf{1}^T \mathbf{X} = \mathbf{1}. \end{aligned} \quad (6)$$

Note that (3) is equivalent to (6) if we skip the sum-to-one constraint. However, combining \mathbf{X} and \mathbf{s} into a nonnegative least squares problem would lose some prior information on \mathbf{X} itself, especially when \mathbf{X} and \mathbf{s} are independent. In the following, we will utilize the prior information and propose a robust optimization framework under a low exposure time measurement.

B. Model-based approach: TV regularization

TV regularization is a widely-used technique in image processing to promote sparsity in the gradient of the image [41, 42]. Here the chemical phase map can be regarded as a group of images and have a piece-wise spatial correlation. Hence, we first adapt TV regularization into (6) and the proposed model can be expressed as follows:

$$\min_{\mathbf{X}, \mathbf{s}} \quad \frac{1}{2} \|\mathbf{Y} - \mathbf{A} \mathbf{X} \text{diag}(\mathbf{s})\|_F^2 + \lambda \sum_{j=1}^L \|\nabla \mathbf{x}_j\|_1 + I_{\Omega_1}(\mathbf{X}) + I_{\Omega_2}(\mathbf{s}), \quad (7)$$

where λ is the regularization parameter, \mathbf{x}_j is the j -th row in the chemical map \mathbf{X} , and the L_1 norm for vectors is denoted by $\|\cdot\|_1$. We define a discrete gradient operator,

$$\nabla \mathbf{z} := \begin{bmatrix} \nabla_x \\ \nabla_y \end{bmatrix} \mathbf{z}, \quad \forall \mathbf{z} \in \mathbb{R}^N,$$

where ∇_x, ∇_y are the finite forward difference operator with a periodic boundary condition in the horizontal and vertical directions, respectively. Here I_{Ω} is the indicator function for the nonnegative value, i.e.,

$$I_{\Omega}(\mathbf{x}) = \begin{cases} 0 & \mathbf{x} \in \Omega, \\ +\infty & \text{otherwise.} \end{cases} \quad (8)$$

In addition, $\Omega_1 = \{\mathbf{X} | \mathbf{X} \geq \mathbf{0} \text{ and } \mathbf{1}^T \mathbf{X} = \mathbf{1}\}$ and $\Omega_2 = \{\mathbf{s} | \mathbf{s} \geq \mathbf{0}\}$. After splitting the variables, the problem in (7) with auxiliary variables can be expressed as follows:

$$\begin{aligned} \min_{\mathbf{X}, \mathbf{s}} \quad & \frac{1}{2} \|\mathbf{Y} - \mathbf{A} \mathbf{M}\|_F^2 + \lambda \sum_{j=1}^L \|\mathbf{u}_j\|_1 + I_{\Omega_1}(\mathbf{W}) + I_{\Omega_2}(\mathbf{t}) \\ \text{s.t.} \quad & \mathbf{M} = \mathbf{X} \text{diag}(\mathbf{s}), \mathbf{W} = \mathbf{X}, \mathbf{t} = \mathbf{s}, \\ & \mathbf{u}_j = \nabla \mathbf{x}_j, \text{ for } j = 1, \dots, L. \end{aligned} \quad (9)$$

Denote $\mathbf{U} = [\mathbf{u}_1, \mathbf{u}_2, \dots, \mathbf{u}_L]$, the corresponding augmented Lagrangian is:

$$\begin{aligned} \mathcal{L}_1(\mathbf{X}, \mathbf{s}, \mathbf{M}, \mathbf{U}, \mathbf{W}, \mathbf{t}, \mathbf{F}) &= \frac{1}{2} \|\mathbf{Y} - \mathbf{A} \mathbf{M}\|_F^2 + \lambda \sum_{j=1}^L \|\mathbf{u}_j\|_1 + I_{\Omega_1}(\mathbf{W}) + I_{\Omega_2}(\mathbf{t}) \\ &+ \frac{\rho}{2} \|\mathbf{X} \text{diag}(\mathbf{s}) - \mathbf{M} + \mathbf{C}\|_F^2 - \frac{\rho}{2} \|\mathbf{C}\|_F^2 \\ &+ \frac{\rho}{2} \sum_{j=1}^L (\|\nabla \mathbf{x}_j - \mathbf{u}_j + \mathbf{d}_j\|_F^2 - \|\mathbf{d}_j\|_F^2) \\ &+ \frac{\rho}{2} \|\mathbf{X} - \mathbf{W} + \mathbf{E}\|_F^2 - \frac{\rho}{2} \|\mathbf{E}\|_F^2 \\ &+ \frac{\rho}{2} \|\mathbf{s} - \mathbf{t} + \mathbf{g}\|_F^2 - \frac{\rho}{2} \|\mathbf{g}\|_F^2, \end{aligned} \quad (10)$$

where $\mathbf{C}, \mathbf{D} = [\mathbf{d}_1, \mathbf{d}_2, \dots, \mathbf{d}_L]$, \mathbf{E}, \mathbf{g} are dual variables and λ, ρ are positive parameters. Denote $\mathbf{F} = [\mathbf{C}; \mathbf{D}; \mathbf{E}; \text{diag}(\mathbf{g})]$.

We apply ADMM as the following scheme,

$$\begin{cases} \mathbf{X}^{k+1} = \arg \min_{\mathbf{X}} \mathcal{L}_1(\mathbf{X}, \mathbf{s}^k, \mathbf{M}^k, \mathbf{U}^k, \mathbf{W}^k, \mathbf{t}^k, \mathbf{F}^k), \\ \mathbf{s}^{k+1} = \arg \min_{\mathbf{s}} \mathcal{L}_1(\mathbf{X}^{k+1}, \mathbf{s}, \mathbf{M}^k, \mathbf{U}^k, \mathbf{W}^k, \mathbf{t}^k, \mathbf{F}^k), \\ \mathbf{M}^{k+1} = \arg \min_{\mathbf{M}} \mathcal{L}_1(\mathbf{X}^{k+1}, \mathbf{s}^{k+1}, \mathbf{M}, \mathbf{U}^k, \mathbf{W}^k, \mathbf{t}^k, \mathbf{F}^k), \\ \mathbf{U}^{k+1} = \arg \min_{\mathbf{U}} \mathcal{L}_1(\mathbf{X}^{k+1}, \mathbf{s}^{k+1}, \mathbf{M}^{k+1}, \mathbf{U}, \mathbf{W}^k, \mathbf{t}^k, \mathbf{F}^k), \\ \mathbf{W}^{k+1} = \arg \min_{\mathbf{W}} \mathcal{L}_1(\mathbf{X}^{k+1}, \mathbf{s}^{k+1}, \mathbf{M}^{k+1}, \mathbf{U}^{k+1}, \mathbf{W}, \mathbf{t}^k, \mathbf{F}^k), \\ \mathbf{t}^{k+1} = \arg \min_{\mathbf{t}} \mathcal{L}_1(\mathbf{X}^{k+1}, \mathbf{s}^{k+1}, \mathbf{M}^{k+1}, \mathbf{U}^{k+1}, \mathbf{W}^{k+1}, \mathbf{t}, \mathbf{F}^k), \\ \mathbf{C}^{k+1} = \mathbf{C}^k + \mathbf{X}^{k+1} \text{diag}(\mathbf{s}^{k+1}) - \mathbf{M}^{k+1}, \\ \mathbf{d}_j^{k+1} = \mathbf{d}_j^k + \nabla \mathbf{x}_j^{k+1} - \mathbf{u}_j^{k+1}, \text{ for } j = 1, \dots, L, \\ \mathbf{E}^{k+1} = \mathbf{E}^k + \mathbf{X}^{k+1} - \mathbf{W}^{k+1}, \\ \mathbf{g}^{k+1} = \mathbf{g}^k + \mathbf{s}^{k+1} - \mathbf{t}^{k+1}, \\ \mathbf{F}^{k+1} = [\mathbf{C}^{k+1}; \mathbf{D}^{k+1}; \mathbf{E}^{k+1}; \text{diag}(\mathbf{g}^{k+1})]. \end{cases} \quad (11)$$

We then elaborate on how to solve the six subproblems in (11), by taking the derivative of \mathcal{L}_1 with respect to \mathbf{X} , we obtain a closed-form solution,

$$\begin{aligned} \mathbf{X}^{k+1} = & ((\mathbf{M}^k - \mathbf{C}^k) \text{diag}(\mathbf{s}^k) + \sum_{j=1}^L \nabla^T (\mathbf{u}_j^k - \mathbf{d}_j^k) \\ & + \mathbf{W}^k - \mathbf{E}^k) (\text{diag}(\mathbf{s}^k)^2 - \Delta + \mathbf{I})^{-1}, \end{aligned} \quad (12)$$

where $\Delta = -\nabla^T \nabla$ represents the Laplacian operator. To solve for (12), we use the conjugate gradient (CG) descent iterations. The \mathbf{s} -subproblem in (11) has a closed-form solution.

$$\mathbf{s}^{k+1} = ((\mathbf{X}^{k+1})^T \mathbf{X}^{k+1} + \mathbf{I})^{-1} ((\mathbf{X}^{k+1})^T (\mathbf{M}^k - \mathbf{C}^k) + \mathbf{t}^k - \mathbf{g}^k). \quad (13)$$

The \mathbf{M} -subproblem in (11) also has a closed-form solution, i.e.,

$$\mathbf{M}^{k+1} = (\mathbf{A}^T \mathbf{A} + \rho \mathbf{I})^{-1} (\mathbf{A}^T \mathbf{Y} + \rho \mathbf{X}^{k+1} \text{diag}(\mathbf{s}^{k+1}) + \rho \mathbf{C}^k). \quad (14)$$

To obtain the \mathbf{U} -subproblem, we take the derivative of \mathcal{L}_1 with respect to \mathbf{u}_j .

$$\mathbf{u}_j^{k+1} = \text{shrink}(\nabla \mathbf{x}_j^{k+1} + \mathbf{d}_j^k, \frac{\lambda}{\rho}), \text{ for } j = 1, \dots, L, \quad (15)$$

where $\text{shrink}(x, \lambda) = \text{sign}(x) \max(|x| - \lambda, 0)$. Here we impose the sum-to-one constraint by normalizing \mathbf{X} in each iteration, then the subproblem of \mathbf{W} and \mathbf{t} are only for the non-negativity-constrained projection operator. Algorithm 1 summarizes the whole process for solving model (10).

C. Learning-based approach: PnP Priors

Designing a powerful regularizer can be challenging, as complex regularizers often complicate optimization problems, making the entire process more difficult. Rather than using a handcrafted regularizer, we aim to leverage prior knowledge about the spectral characteristics of materials in the scene to achieve better regularized unmixing results. Our proposed method can be seamlessly integrated into existing optimization frameworks, making it a practical and efficient tool for

Algorithm 1 The Framework for XANES Image Unmixing with TV Regularization and PnP Priors.

Input: A XANES image \mathbf{Y} , Dictionary \mathbf{A} .

Output: Phase map \mathbf{X} , Scaling factor \mathbf{s} .

- 1: Initialize: \mathbf{X} and \mathbf{s} and choose parameter ρ and λ .
 - 2: **while** not converged or iterations are not reached **do**
 - 3: $\mathbf{X} \leftarrow \begin{cases} \text{is updated by (12) for TV,} \\ \text{is updated by (19) for PnP,} \end{cases}$
 - 4: Normalize \mathbf{X} such that $\mathbf{1}^T \mathbf{X} = \mathbf{1}$,
 - 5: $\mathbf{s} \leftarrow (\mathbf{X}^T \mathbf{X} + \mathbf{I})^{-1} (\mathbf{X}^T (\mathbf{M} - \mathbf{C}) + \mathbf{t} - \mathbf{g})$,
 - 6: $\mathbf{M} \leftarrow (\mathbf{A}^T \mathbf{A} + \rho \mathbf{I})^{-1} (\mathbf{A}^T \mathbf{Y} + \rho \mathbf{X} \text{diag}(\mathbf{s}) + \rho \mathbf{C})$,
 - 7: $\mathbf{U} \leftarrow \begin{cases} \text{shrink}(\nabla \mathbf{x}_j + \mathbf{d}_j, \frac{\lambda}{\rho}), & \text{for TV} \\ \text{Denoiser}(\mathbf{x}_j + \mathbf{d}_j, \frac{\lambda}{\rho}), & \text{for PnP} \end{cases}$
 - 8: $\mathbf{W} \leftarrow \max(\mathbf{X} + \mathbf{E}, \mathbf{0})$,
 - 9: $\mathbf{t} \leftarrow \max(\mathbf{s} + \mathbf{g}, \mathbf{0})$,
 - 10: $\mathbf{C} \leftarrow \mathbf{C} + \mathbf{X} \text{diag}(\mathbf{s}) - \mathbf{M}$,
 - 11: $\mathbf{d}_j \leftarrow \begin{cases} \mathbf{d}_j + \nabla \mathbf{x}_j - \mathbf{u}_j, & \text{for TV} \\ \mathbf{d}_j + \mathbf{x}_j - \mathbf{u}_j, & \text{for PnP} \end{cases}$
 - 12: $\mathbf{E} \leftarrow \mathbf{E} + \mathbf{X} - \mathbf{W}$,
 - 13: $\mathbf{g} \leftarrow \mathbf{g} + \mathbf{s} - \mathbf{t}$.
 - 14: **end while**
-

XANES image unmixing. The optimization problem can be formulated as follows:

$$\min_{\mathbf{X}, \mathbf{s}} \frac{1}{2} \|\mathbf{Y} - \mathbf{A} \mathbf{X} \text{diag}(\mathbf{s})\|_F^2 + \lambda \sum_{j=1}^L \Phi(\mathbf{x}_j) + I_{\Omega_1}(\mathbf{X}) + I_{\Omega_2}(\mathbf{s}), \quad (16)$$

where $\Phi(\mathbf{X})$ represents some regularization term enforcing prior knowledge of \mathbf{X} .

By introducing the auxiliary variables, the optimization problem of (16) can be written in the equivalent form:

$$\begin{aligned} \min_{\mathbf{X}, \mathbf{s}} \quad & \frac{1}{2} \|\mathbf{Y} - \mathbf{A} \mathbf{M}\|_F^2 + \lambda \sum_{j=1}^L \Phi(\mathbf{u}_j) + I_{\Omega_1}(\mathbf{W}) + I_{\Omega_2}(\mathbf{t}) \\ \text{s.t.} \quad & \mathbf{M} = \mathbf{X} \text{diag}(\mathbf{s}), \mathbf{u}_j = \mathbf{x}_j, \mathbf{W} = \mathbf{X}, \mathbf{t} = \mathbf{s}. \end{aligned} \quad (17)$$

and the augmented Lagrangian is as follows:

$$\begin{aligned} \mathcal{L}_2(\mathbf{X}, \mathbf{s}, \mathbf{M}, \mathbf{U}, \mathbf{W}, \mathbf{t}, \mathbf{F}) &= \frac{1}{2} \|\mathbf{Y} - \mathbf{A} \mathbf{M}\|_F^2 + \lambda \sum_{j=1}^L \Phi(\mathbf{u}_j) \\ &+ \frac{\rho}{2} \|\mathbf{X} \text{diag}(\mathbf{s}) - \mathbf{M} + \mathbf{C}\|_F^2 - \frac{\rho}{2} \|\mathbf{C}\|_F^2 \\ &+ \frac{\rho}{2} \sum_{j=1}^L \|\mathbf{x}_j - \mathbf{u}_j + \mathbf{d}_j\|_F^2 - \frac{\rho}{2} \|\mathbf{d}_j\|_F^2 \\ &+ \frac{\rho}{2} \|\mathbf{X} - \mathbf{W} + \mathbf{E}\|_F^2 - \frac{\rho}{2} \|\mathbf{E}\|_F^2 \\ &+ \frac{\rho}{2} \|\mathbf{s} - \mathbf{t} + \mathbf{g}\|_F^2 - \frac{\rho}{2} \|\mathbf{g}\|_F^2, \end{aligned} \quad (18)$$

where \mathbf{C} , \mathbf{D} , \mathbf{E} , \mathbf{g} are dual variables and λ , ρ are positive parameters. The method for solving model (18) is similar to

that of model (10). Specifically, by taking the derivative of \mathcal{L}_2 with respect to \mathbf{X} , the \mathbf{X} -subproblem has a closed-form solution.

$$\begin{aligned} \mathbf{X}^{k+1} = & ((\mathbf{M}^k - \mathbf{C}^k)\text{diag}(\mathbf{s}^k) + \sum_{j=1}^L (\mathbf{u}_j^k - \mathbf{d}_j^k) \\ & + \mathbf{W}^k - \mathbf{E}^k)(\text{diag}(\mathbf{s}^k)^2 + 2\mathbf{I})^{-1}. \end{aligned} \quad (19)$$

The \mathbf{u}_j -subproblem is to solve a proximal proximal operator as follows:

$$\mathbf{u}_j^{k+1} = \arg \min_{\mathbf{u}} \frac{\rho}{2} \|\mathbf{u} - \mathbf{x}_j^{k+1} - \mathbf{d}_j^k\|_F^2 + \lambda\phi(\mathbf{u}), \quad (20)$$

which can be viewed as an image-denoising problem. The goal is to eliminate additive Gaussian noise with a standard deviation of $\sigma = \sqrt{\lambda/\rho}$. We employ established and effective denoising operators in the PnP framework iterations, such as the conventional BM3D [43] or DnCNN [44], which utilizes deep learning. After acquiring the necessary denoising operators, we update the primal and dual variables in the ADMM process, following Algorithm 1.

Remark 1. *Dictionary selection: The proposed algorithm can quickly and accurately extract the spectral signal from the XANES imaging data. However, the reference spectra are a critical component for achieving optimal performance. When the reference spectra are unknown, we use the conventional spectra extraction method, which is the vertex component analysis (VCA) [45] as a baseline for dictionary identification. In the real data analysis in Section V-D, we demonstrate that using VCA with denoising results in more accurate reference spectra extraction, particularly in strong-noise environments.*

IV. CONVERGENCE ANALYSIS

In this section, we demonstrate the convergence of Algorithm 1 with TV regularization. Under some assumptions, we prove an optimal solution to the problem (10) can be found by iterating the scheme (11). Although this result is not entirely satisfactory, it provides some theoretical guarantees for the reliability of Algorithm 1 with TV regularization.

Assuming $\mathcal{X}^* = \{\mathbf{X}^*, \mathbf{s}^*, \mathbf{M}^*, \mathbf{U}^*, \mathbf{W}^*, \mathbf{t}^*, \mathbf{C}^*, \mathbf{D}^*, \mathbf{E}^*, \mathbf{g}^*\}$ as the fixed point, then the Karush-Kuhn-Tucker (KKT) condition of (9) can be summarized as follows:

$$\left\{ \begin{array}{l} \mathbf{0} = \mathbf{M}^* - \mathbf{X}^* \text{diag}(\mathbf{s}^*), \\ \mathbf{0} = \mathbf{u}_j^* - \nabla \mathbf{x}_j^*, \text{ for } j = 1, \dots, L, \\ \mathbf{0} = \mathbf{W}^* - \mathbf{X}^*, \\ \mathbf{0} = \mathbf{t}^* - \mathbf{s}^*, \\ \mathbf{0} = \mathbf{C}^* \text{diag}(\mathbf{s}^*) + \sum_{j=1}^L \nabla^T \mathbf{d}_j^* + \mathbf{E}^*, \\ \mathbf{0} = \mathbf{X}^{*T} \mathbf{C}^* + \rho \text{diag}(\mathbf{g}^*), \\ \mathbf{0} = \mathbf{A}^T (\mathbf{Y} - \mathbf{A} \mathbf{M}^*) - \rho \mathbf{C}^*, \\ \mathbf{0} \in \lambda \partial \|\mathbf{u}_j^*\|_1 - \rho \mathbf{d}_j^*, \text{ for } j = 1, \dots, L, \\ \langle \mathbf{E}^*, \mathbf{W} - \mathbf{W}^* \rangle \leq 0 \quad \forall \mathbf{W} \in \Omega_1, \\ \langle \mathbf{g}^*, \mathbf{t} - \mathbf{t}^* \rangle \leq 0 \quad \forall \mathbf{t} \in \Omega_2. \end{array} \right. \quad (21)$$

Theorem 1. *Let \mathcal{X}^k be generated by Algorithm 1, if the successive differences of the multipliers $\mathbf{C}^{k+1} - \mathbf{C}^k$, $\mathbf{D}^{k+1} - \mathbf{D}^k$, $\mathbf{E}^{k+1} - \mathbf{E}^k$ and $\mathbf{g}^{k+1} - \mathbf{g}^k$ all converges to $\mathbf{0}$ as k tends to ∞ , and if $\{\mathbf{s}^k\}$ is bounded, then there exists a subsequence*

\mathcal{X}^{k_j} whose accumulation point satisfies the KKT condition of (9).

Proof. Since $\lim_{k \rightarrow \infty} \mathbf{C}^{k+1} - \mathbf{C}^k = \mathbf{0}$ and $\lim_{k \rightarrow \infty} \mathbf{D}^{k+1} - \mathbf{D}^k = \mathbf{0}$, and the multiplier updates are given by (11), it can be conclude that

$$\begin{aligned} \lim_{k \rightarrow \infty} \mathbf{X}^k \text{diag}(\mathbf{s}^k) - \mathbf{M}^k &= \mathbf{0}, \\ \lim_{k \rightarrow \infty} \nabla \mathbf{x}_j^k - \mathbf{u}_j^k &= \mathbf{0}, \text{ for } j = 1, \dots, L. \end{aligned} \quad (22)$$

Here \mathbf{W}^k is bounded owing to the constraint Ω_1 . Incorporating $\lim_{k \rightarrow \infty} \mathbf{E}^{k+1} - \mathbf{E}^k = \mathbf{0}$, we get the boundedness of \mathbf{X}^k . Hence there exists a bounded subsequence such that $\lim_{j \rightarrow \infty} \mathbf{E}^{k_j} = \lim_{j \rightarrow \infty} \mathbf{X}^{k_j} = \mathbf{X}^*$. It can be inferred that both \mathbf{M}^k , \mathbf{U}^k , and \mathbf{t} are bounded from the same analysis. Therefore, the following system of equations holds:

$$\left\{ \begin{array}{l} \mathbf{X}^* \text{diag}(\mathbf{s}^*) = \mathbf{M}^*, \\ \nabla \mathbf{x}_j^* = \mathbf{u}_j^*, \text{ for } j = 1, \dots, L, \\ \mathbf{W}^* = \mathbf{X}^*, \\ \mathbf{t}^* = \mathbf{s}^*. \end{array} \right. \quad (23)$$

The optimality condition associated with \mathbf{X} -subproblem can be written as:

$$\begin{aligned} (\mathbf{X}^* \text{diag}(\mathbf{s}^*) - \mathbf{M}^* + \mathbf{C}^*) \text{diag}(\mathbf{s}^*) + \sum_{j=1}^L \nabla^T (\nabla \mathbf{x}_j^* - \mathbf{u}_j^* \\ + \mathbf{d}_j^*) + (\mathbf{X}^* - \mathbf{W}^* + \mathbf{E}^*) = \mathbf{0}. \end{aligned} \quad (24)$$

Using (23), we have:

$$\mathbf{C}^* \text{diag}(\mathbf{s}^*) + \sum_{j=1}^L \nabla^T \mathbf{d}_j^* + \mathbf{E}^* = \mathbf{0}. \quad (25)$$

Similarly, by the optimality conditions associated with \mathbf{s} and \mathbf{M} -subproblems, we obtain

$$\left\{ \begin{array}{l} \mathbf{X}^{*T} \mathbf{C}^* + \rho \text{diag}(\mathbf{g}^*) = \mathbf{0}, \\ \mathbf{A}^T (\mathbf{Y} - \mathbf{A} \mathbf{M}^*) - \rho \mathbf{C}^* = \mathbf{0}. \end{array} \right. \quad (26)$$

The proof of the final relationship on the stationary condition in (21) can be found in [46], the specific proof of the relationship is omitted here. Lastly, from optimality condition in the \mathbf{W} -subproblem in (11) we get

$$\begin{aligned} \langle -\mathbf{E}^k, \mathbf{W} - \mathbf{W}^{k+1} \rangle &\geq -\langle \mathbf{W}^{k+1} - \mathbf{X}^{k+1}, \mathbf{W} - \mathbf{W}^{k+1} \rangle \\ &\geq -\|\mathbf{W}^{k+1} - \mathbf{X}^{k+1}\| \|\mathbf{W} - \mathbf{W}^{k+1}\|, \quad \forall \mathbf{W} \in \Omega_1, \\ \langle -\mathbf{g}^k, \mathbf{t} - \mathbf{t}^{k+1} \rangle &\geq -\langle \mathbf{t}^{k+1} - \mathbf{s}^{k+1}, \mathbf{t} - \mathbf{t}^{k+1} \rangle \\ &\geq -\|\mathbf{t}^{k+1} - \mathbf{s}^{k+1}\| \|\mathbf{t} - \mathbf{t}^{k+1}\|, \quad \forall \mathbf{g} \in \Omega_2. \end{aligned}$$

Thus, we have

$$\begin{aligned} \langle \mathbf{E}^*, \mathbf{W} - \mathbf{W}^* \rangle &\leq 0 \quad \forall \mathbf{W} \geq \mathbf{0}, \\ \langle \mathbf{g}^*, \mathbf{t} - \mathbf{t}^* \rangle &\leq 0 \quad \forall \mathbf{g} \geq \mathbf{0}. \end{aligned}$$

□

Remark 2. *Note that (7) is a non-convex optimization problem with respect to both \mathbf{X} and \mathbf{s} , and our algorithm (11) is a four-block ADMM. The corresponding convergence analysis is very challenging. We refer to some existing work [46–48] and establish the convergence under the assumption of the successive differences of the multipliers, which is empirically verified in Section V.*

V. EXPERIMENTS AND RESULTS

In this section, we will evaluate the performance of the proposed methods quantitatively and visually on both synthetic and actual datasets. Regarding the comparison with different priors, our methods were divided into two groups: the model-based method (RUM_{TV}) and learning-based methods ($\text{RUM}_{\text{PnP}_1}$ denotes as PnP with DnCNN [44], $\text{RUM}_{\text{PnP}_2}$ denotes as PnP with BM3D [43]). These proposed methods will be assessed in comparison to the traditional methods, namely edge-50 and LCF.

A. Experimental Settings and Evaluation Metrics

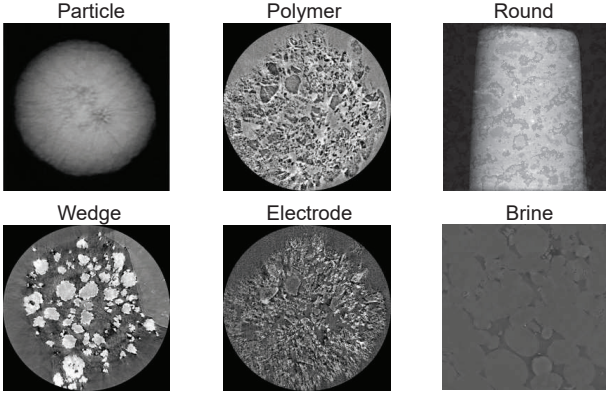


Fig. 2. Typical examples of the test datasets: projections (top) and reconstructed slices (bottom).

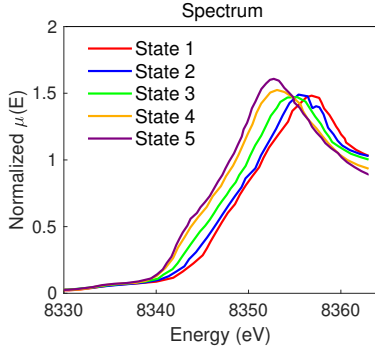


Fig. 3. Normalized spectra under different Ni valence states of X-ray XANES in a battery cathode. State 1, 2, 3, 4, 5 represent the different valence states of Ni, respectively.

Data Description. The dataset presented in Fig. 2 comprises three X-ray projection images (Particles, Polymer and Round) and three reconstructed slices (Wedge, Electrode and Brine), which were utilized to create a simulation of 2D and 3D TXM-XANES imaging scenarios. To generate simulated movie data, as shown in Fig. 3, the reference spectra of different Ni valence states were randomly assigned to pixels in the images for various phase maps. The sample is assumed to contain various valence states of Ni elements, and the proportion of Ni elements satisfies the sum-to-one constraint. We use number $(1, 2, 3, \dots, L)$ to describe the state.

Evaluation Metrics. Each synthetic dataset frame is further corrupted with additive Gaussian noise with varying noise levels, with the standard deviation $\sigma \in [1, 7]$. For the performance assessment of the algorithms, we utilize two commonly used criteria to measure the accuracy of the phase map: the peak signal-to-noise ratio (PSNR) and the structural similarity index (SSIM). PSNR is defined as follows:

$$\text{PSNR} = 20 \times \log_{10} (\text{MAX}/\text{RMSE}), \quad (27)$$

where MAX is the maximum pixel value of the estimated image $\hat{\mathbf{X}}$, and RMSE is the root mean square error between $\hat{\mathbf{X}}$ and the ground truth \mathbf{X} . The RMSE is defined as:

$$\text{RMSE} = \sqrt{\frac{1}{n_1 n_2} \sum_{i=1}^{n_1} \sum_{j=1}^{n_2} \|\hat{x}(i, j) - x(i, j)\|^2}, \quad (28)$$

where n_1 and n_2 are the number of rows and columns in the image \mathbf{X} . We use the estimated phase map $\hat{\mathbf{X}}$ and the ground truth \mathbf{X} to calculate PSNR.

SSIM is a metric that quantifies the similarity between two images. The SSIM formula is expressed as follows:

$$\text{SSIM}(\hat{\mathbf{X}}, \mathbf{X}) = \frac{[(2\mu_{\hat{\mathbf{X}}}\mu_{\mathbf{X}} + c_1) * (2\sigma_{\hat{\mathbf{X}}\mathbf{X}} + c_2)]}{[(\mu_{\hat{\mathbf{X}}}^2 + \mu_{\mathbf{X}}^2 + c_1) * (\sigma_{\hat{\mathbf{X}}}^2 + \sigma_{\mathbf{X}}^2 + c_2)]}, \quad (29)$$

where $\mu_{\hat{\mathbf{X}}}$ and $\mu_{\mathbf{X}}$ represent the means of $\hat{\mathbf{X}}$ and \mathbf{X} , respectively. $\sigma_{\hat{\mathbf{X}}}$ and $\sigma_{\mathbf{X}}$ denote the standard deviations of $\hat{\mathbf{X}}$ and \mathbf{X} , respectively. $\sigma_{\hat{\mathbf{X}}\mathbf{X}}$ is the covariance of $\hat{\mathbf{X}}$ and \mathbf{X} , while c_1 and c_2 are small constants added to prevent division by zero errors and stabilize the formula.

Parameter Settings. The maximum iteration of the RUM algorithm is set as 100 for all scenarios. To achieve the best RMSE results for simulated data, λ and ρ are fine-tuned for various methods. Fig. 4 illustrates the effect of parameters ρ and λ on the performance of RUM_{TV} using Particle data with $\sigma = 3$. We observe that λ regulates the influence of the regularization term and significantly affects the unmixing results, whereas ρ is a penalty parameter in the augmented Lagrangian function and only affects the convergence speed.

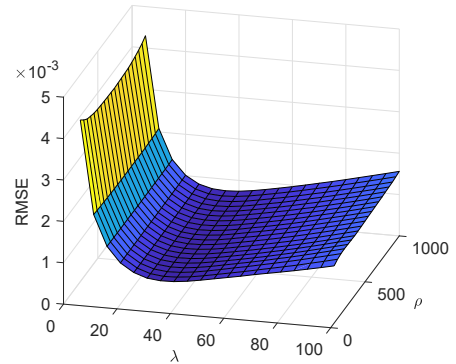


Fig. 4. The study analyzed the relationship between RMSE and regularization parameters using Particle data ($\sigma = 3$) and evaluated the performance of the RUM_{TV} method.

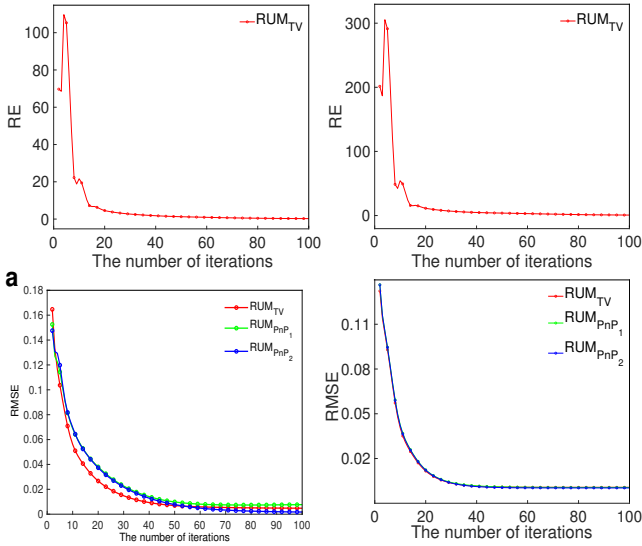


Fig. 5. The RE and RMSE curves of our proposed methods were analyzed using the Particle (left) data and the Brine data (right) under the noise level $\sigma = 3$.

B. Analysis of the proposed algorithm

Convergence. In Section IV, we have proved the convergence analysis on Algorithm 1 with the TV regularization under some assumptions. Here we conduct experiments to empirically verify the assumption and demonstrate the convergence outcomes of three proposed methods with both TV and PnP priors. For each iteration, we plot the relative errors (RE) defined as $\|\mathbf{C}^{k+1} - \mathbf{C}^k\|_F^2 + \|\mathbf{D}^{k+1} - \mathbf{D}^k\|_F^2 + \|\mathbf{E}^{k+1} - \mathbf{E}^k\|_F^2 + \|\mathbf{g}^{k+1} - \mathbf{g}^k\|_F^2$ to verify the assumption in Theorem 1. In addition, we also plot the RMSE in (28) with respect to the iteration. Fig. 5 shows that the value of RE goes to zero during the iteration, which is consistent with the assumption in Theorem 1. Three methods achieve stable RMSE values after 100 outer iterations on both datasets. Hence we set the maximum iteration number as 100 in the following experiment to reduce the computation time.

TABLE I

Comparison of the computational time (units: seconds). Particle and Brine data have the image size of $379 \times 520 \times 969$ and $761 \times 742 \times 969$, respectively.

| | Edge-50 | LCF | RUM _{TV} | RUM _{PnP1} | RUM _{PnP2} |
|----------|--------------|-------|-------------------|---------------------|---------------------|
| Particle | 2.40 | 4.11 | 9.78 | 13.51 | 210.54 |
| Brine | 10.97 | 31.40 | 42.20 | 46.72 | 333.59 |

Running Time. In order to find a balance between performance improvement and computational efficiency, we conducted experiments to evaluate the running times of various datasets on the CPU. It is worth noting that all of these experiments were conducted on a computer equipped with an Intel i7-6348 2.6 GHz CPU and 16 GB of RAM. Table I shows the average computation time for the Particle and Brine datasets. The edge-50 method requires the least amount of time because it does not require any iterative computation. RUM_{TV} is much smaller than the other priors. In particular, when the

data size is larger, the running time of RUM with DnCNN is much smaller than BM3D. Our observations indicate that the running time of the proposed framework depends mainly on the complexity of the different priors.

Selection of the PnP prior. The proposed PnP framework offers great flexibility, allowing us to incorporate various state-of-the-art image-denoising approaches. This study examines two notable denoisers: DnCNN [44] and BM3D [43]. The results in Table II demonstrate that both methods significantly enhance the PSNRs and SSIMs across different datasets. However, when observing Fig. 6, it becomes evident that RUM with BM3D achieves superior outcomes. Therefore, we employ BM3D as our chosen denoising approach for the following experiments, referred to as RUM_{PnP}.

TABLE II

Comparison of PSNR (dB) and SSIM for two datasets using different PnP priors ($\sigma = 3$).

| | Particle | | Brine | |
|------------------|--------------|-------------|--------------|-------------|
| | PSNR | SSIM | PSNR | SSIM |
| PnP ₁ | 33.20 | 0.84 | 34.51 | 0.78 |
| PnP ₂ | 37.36 | 0.96 | 39.85 | 0.94 |

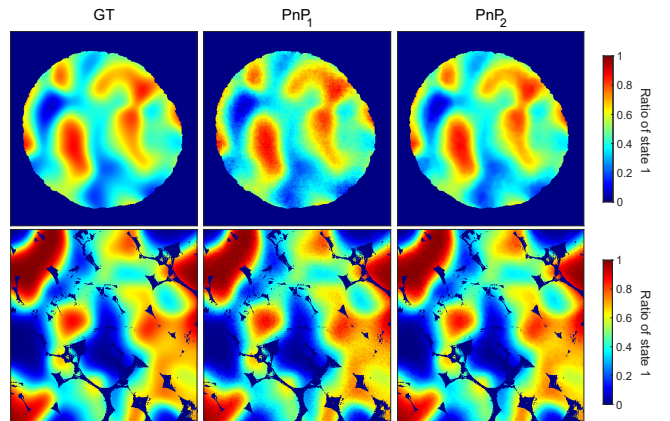


Fig. 6. A visual comparison of the chemical phase map for the different PnP priors on the Particle data (top) and the Brine data (bottom) when $\sigma = 3$.

C. Results of synthetic datasets

Different Noise Levels. Table III displays the performance of both traditional methods and our proposed unmixing methods incorporating TV and PnP priors with two reference spectra. The optimal results are highlighted in bold font. Overall, our two methods all outperform the traditional techniques for all the datasets. They exhibit remarkable robustness to a wide range of noise levels, particularly when the noise is substantial, as the chemical map is still reconstructed effectively. RUM_{PnP} performs best under all noise conditions. In Fig. 7, we compare the chemical phase maps of Round data obtained from various approaches under two kinds of noise levels. Except for edge-50, we observe that the estimated phase maps are consistent with the ground truth. However, under strong noise, our proposed methods yield less noisy phase maps closer to the

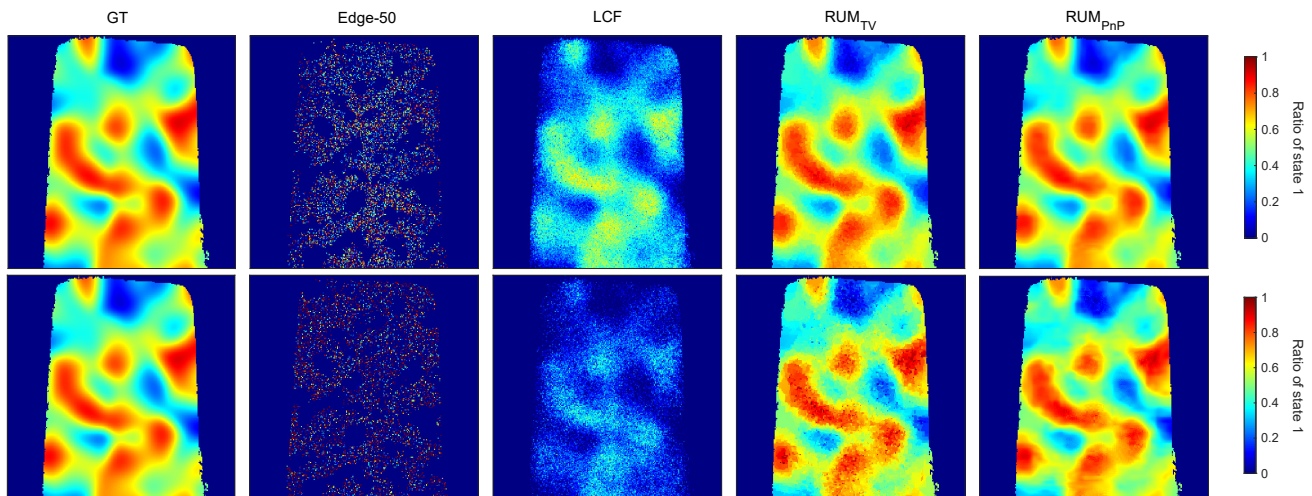


Fig. 7. A visual comparison of the chemical phase map for various methods on the Round data under different noise levels ($\sigma = 3$ on the top and $\sigma = 7$ on the bottom). Note that the other chemical map is the reverse since $L = 2$.

TABLE III
Comparison of PSNR (dB) and SSIM for simulated datasets using different approaches and noise levels.

| Test set | σ | Edge-50 | | LCF | | RUM _{TV} | | RUM _{PnP} | |
|-----------|----------|---------|------|-------|------|-------------------|------|--------------------|-------------|
| | | PSNR | SSIM | PSNR | SSIM | PSNR | SSIM | PSNR | SSIM |
| Particle | 1 | 8.98 | 0.10 | 16.11 | 0.57 | 38.22 | 0.94 | 42.65 | 0.98 |
| | 3 | 5.96 | 0.08 | 9.33 | 0.28 | 32.64 | 0.87 | 37.36 | 0.96 |
| | 5 | 5.73 | 0.07 | 6.80 | 0.22 | 29.59 | 0.76 | 34.39 | 0.93 |
| | 7 | 5.71 | 0.07 | 5.26 | 0.20 | 27.63 | 0.69 | 31.39 | 0.87 |
| Electrode | 1 | 9.19 | 0.23 | 17.37 | 0.51 | 42.39 | 0.95 | 46.79 | 0.99 |
| | 3 | 6.23 | 0.22 | 10.00 | 0.36 | 38.38 | 0.92 | 42.27 | 0.98 |
| | 5 | 6.01 | 0.22 | 7.29 | 0.35 | 33.65 | 0.83 | 37.97 | 0.95 |
| | 7 | 5.97 | 0.21 | 6.03 | 0.36 | 31.51 | 0.78 | 35.21 | 0.92 |
| Polymer | 1 | 11.20 | 0.23 | 19.94 | 0.59 | 42.36 | 0.95 | 47.10 | 0.99 |
| | 3 | 6.56 | 0.22 | 11.86 | 0.39 | 37.85 | 0.89 | 42.74 | 0.98 |
| | 5 | 6.07 | 0.21 | 8.94 | 0.35 | 32.44 | 0.75 | 38.53 | 0.94 |
| | 7 | 5.97 | 0.21 | 7.27 | 0.35 | 30.00 | 0.68 | 34.29 | 0.86 |
| Wedge | 1 | 10.04 | 0.23 | 19.23 | 0.56 | 47.26 | 0.99 | 51.01 | 1.00 |
| | 3 | 6.58 | 0.21 | 10.97 | 0.35 | 38.98 | 0.93 | 43.35 | 0.99 |
| | 5 | 6.23 | 0.21 | 8.15 | 0.34 | 33.65 | 0.83 | 38.14 | 0.95 |
| | 7 | 6.13 | 0.21 | 6.88 | 0.32 | 31.41 | 0.76 | 34.86 | 0.89 |
| Round | 1 | 7.06 | 0.04 | 12.17 | 0.50 | 35.28 | 0.92 | 39.58 | 0.97 |
| | 3 | 4.89 | 0.01 | 6.81 | 0.28 | 28.53 | 0.80 | 34.14 | 0.94 |
| | 5 | 4.66 | 0.01 | 5.06 | 0.22 | 26.35 | 0.70 | 30.78 | 0.88 |
| | 7 | 4.63 | 0.01 | 3.95 | 0.19 | 24.43 | 0.63 | 28.19 | 0.80 |
| Brine | 1 | 10.46 | 0.03 | 19.86 | 0.52 | 40.34 | 0.92 | 45.40 | 0.97 |
| | 3 | 4.96 | 0.01 | 10.54 | 0.24 | 35.59 | 0.83 | 39.85 | 0.94 |
| | 5 | 4.59 | 0.01 | 7.08 | 0.18 | 30.90 | 0.66 | 37.01 | 0.91 |
| | 7 | 4.55 | 0.01 | 5.17 | 0.17 | 28.52 | 0.56 | 33.00 | 0.80 |

ground truth and preserve the image details. The edge-50 and LCF methods are pixel-based and do not consider the spatial-spectral correlations in XANES images. Our proposed RUM_{TV} method employs fixed regularizers and lacks flexibility, while the PnP framework models priors using denoiser, thus eliminating the need for handcrafted regularizers.

Number of reference spectra. To evaluate the capability of unmixing multiple spectra for XANES data, we generated two datasets at reference spectra ($L = 3, 4, 5$) when $\sigma = 3$. Here different reference spectra represent different valence states of Ni. The results of PSNRs and SSIMs are presented in Table IV, demonstrating our proposed framework's robustness and superiority. Additionally, Fig. 8 displays the phase maps of

TABLE IV
Comparison of PSNR (dB) and SSIM using different approaches with varying numbers of the reference spectra ($\sigma = 3$).

| Test set | L | LCF | | RUM _{TV} | | RUM _{PnP} | |
|----------|-----|-------|------|-------------------|------|--------------------|-------------|
| | | PSNR | SSIM | PSNR | SSIM | PSNR | SSIM |
| Particle | 3 | 13.46 | 0.52 | 22.56 | 0.80 | 22.64 | 0.92 |
| | 4 | 13.36 | 0.48 | 20.32 | 0.73 | 21.23 | 0.85 |
| | 5 | 13.72 | 0.48 | 21.31 | 0.76 | 19.45 | 0.89 |
| Wedge | 3 | 11.47 | 0.27 | 24.55 | 0.74 | 26.23 | 0.92 |
| | 4 | 10.66 | 0.24 | 18.05 | 0.61 | 19.34 | 0.75 |
| | 5 | 12.62 | 0.25 | 19.26 | 0.66 | 20.13 | 0.80 |

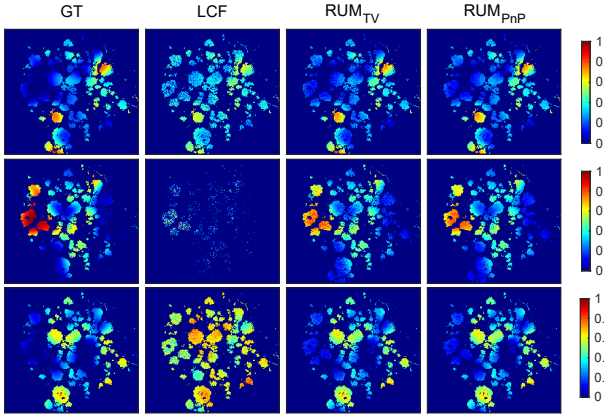


Fig. 8. The visual comparison for the chemical phase maps of the various methods on Wedge data under three reference spectra ($\sigma = 3$). From top to bottom: Ni valence state 1, 2, 3, respectively.

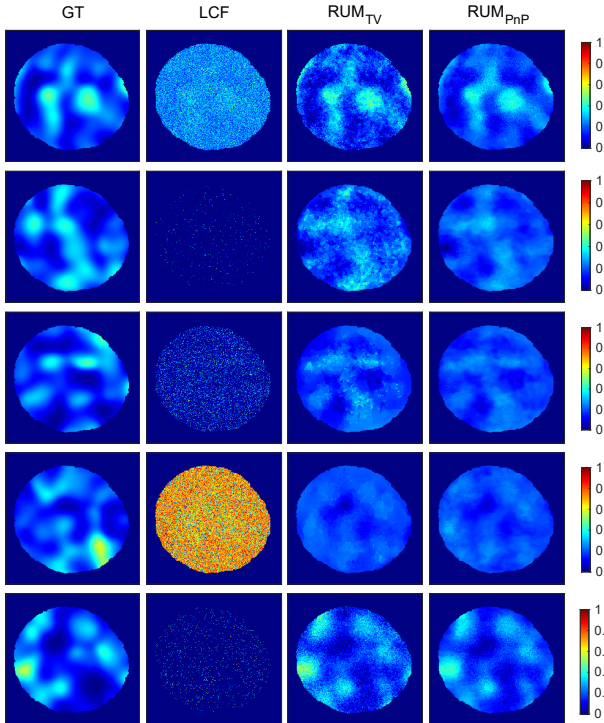


Fig. 9. The visual comparison for the chemical phase maps of the various methods on Particle data under five reference spectra ($\sigma = 3$). From top to bottom: Ni valence state 1, 2, 3, 4, 5, respectively.

three reference spectra using Wedge data, indicating that our phase maps are closer to the ground truth. Furthermore, Fig. 9 shows the result with the number of reference spectra being 5. The phase maps with Particle data for Ni valence state 1, 2, and 5 obtained RUM method exhibit clearer structural details. However, the structure of the phase map for Ni valence state 3 and 4 is not very clear, suggesting a strong correlation between its reference spectra. Nevertheless, RUM_{pnp} still outperforms other methods in unmixing multiple spectra.

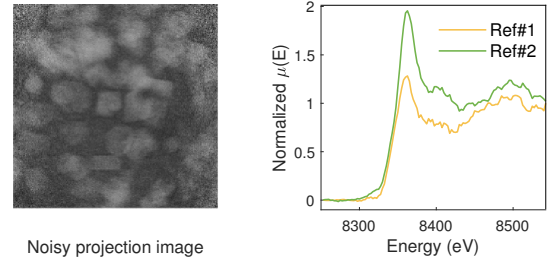


Fig. 10. Low SNR projection image of TXM-XANES recording (left) and the reference spectra dictionary (right).

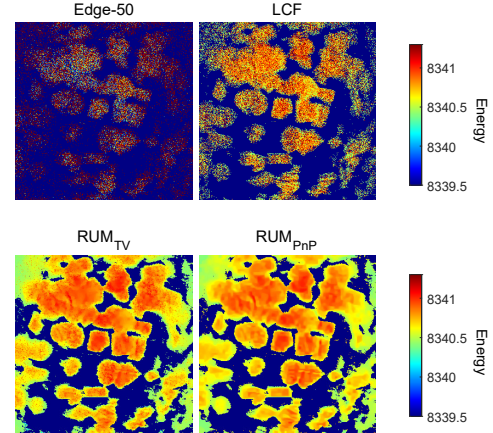


Fig. 11. The chemical state maps, generated from noisy data using various methods, display the energy of the Ni valence state through their colors. Using RUM enhances the interpretability of real data and enables the identification of inter and intra-particle state differences.

D. Results of real dataset

We apply the proposed RUM_{TV} and RUM_{pnp} methods to unmix actual real TXM-XANES data. The data comprises an image of numerous NCM particles on a charged cathode, as shown on the left in Fig. 10. The exposure time for a single frame was 0.5 seconds, and the data was captured at 117 energy points from 8180 eV to 8562 eV.

The NCM particle data exhibits an extremely low signal-to-noise ratio, making it challenging to discern the reference spectra of Ni elements in the range of 8180 eV to 8562 eV under practical conditions. Consequently, we can only determine that it contains Ni at different internal states, similar to the blind unmixing. To address this issue, we employ the denoising algorithm [14] followed by VCA [45] to improve the signal-to-noise ratio and dictionary extraction. We focus on two Ni states where the reference spectra of these states extracted from the range of 8180 eV to 8562 eV are illustrated on the right in Fig. 10. These techniques allowed us to overcome the low signal-to-noise ratio and extract valuable information from the NCM particle data.

As shown in Fig. 11, the proposed RUM algorithms clearly distribute chemical elements in the NCM particle structure. Note that RUM_{TV} has some theoretical guarantee on the convergence while the RUM_{pnp} show better unmixing results in the synthetic experiments. On the other hand, due to the high noise levels in each projection image of NCM particles, the chemical

map obtained using edge-50 and LCF fail to provide any meaningful information. Our methods simultaneously unmix and denoise the chemical imaging data, avoiding the accumulated error if we split these two processes. Additionally, the chemical phase map of NCM particles indicates an uneven reaction of the battery electrode, with some particles exhibiting a higher Ni valence state and others showing a lower Ni valence state. The utilization of the RUM unmixing method opens up avenues for enhanced understanding of spatiotemporally electrochemical reactions, enabling more profound insights and facilitating the optimization of composite electrode designs.

VI. CONCLUSION

This paper introduced a robust spectra unmixing framework to extract the chemical phase map signal for the widely-used X-ray imaging technique. Our proposed framework considered variance in spectra and maximized the use of spatial-spectral priors in X-ray microspectroscopy. It outperforms traditional methods when dealing with strong noise and spectral variability. Additionally, the framework exhibits favorable convergence properties for TV regularization, while the PnP prior performs better. Our future study includes the theoretical analysis of the proposed framework with the PnP prior.

REFERENCES

- [1] F. Meirer, J. Cabana, Y. Liu, A. Mehta, J. C. Andrews, and P. Pianetta, "Three-dimensional imaging of chemical phase transformations at the nanoscale with full-field transmission X-ray microscopy," *Journal of Synchrotron Radiation*, vol. 18, no. 5, pp. 773–781, Jul. 2011. I, II-A
- [2] J. Wang, Y.-c. K. Chen-Wiegart, and J. Wang, "In operando tracking phase transformation evolution of lithium iron phosphate with hard X-ray microscopy," *Nature Communications*, vol. 5, no. 1, p. 4570, Aug. 2014. I
- [3] U. Boesenberg, F. Meirer, Y. Liu, A. K. Shukla, R. Dell'Anna, T. Tylliszczak, G. Chen, J. C. Andrews, T. J. Richardson, R. Kostecki *et al.*, "Mesoscale phase distribution in single particles of LiFePO₄ following lithium deintercalation," *Chemistry of Materials*, vol. 25, no. 9, pp. 1664–1672, Mar. 2013. I
- [4] H. Yang, H.-H. Wu, M. Ge, L. Li, Y. Yuan, Q. Yao, J. Chen, L. Xia, J. Zheng, Z. Chen *et al.*, "Simultaneously dual modification of Ni-rich layered oxide cathode for high-energy lithium-ion batteries," *Advanced Functional Materials*, vol. 29, no. 13, p. 1808825, Feb. 2019.
- [5] K. Zhang, F. Ren, X. Wang, E. Hu, Y. Xu, X.-Q. Yang, H. Li, L. Chen, P. Pianetta, A. Mehta *et al.*, "Finding a needle in the haystack: identification of functionally important minority phases in an operating battery," *Nano Letters*, vol. 17, no. 12, pp. 7782–7788, Nov. 2017. I
- [6] Y. Xu, E. Hu, K. Zhang, X. Wang, V. Borzenets, Z. Sun, P. Pianetta, X. Yu, Y. Liu, X.-Q. Yang *et al.*, "In situ visualization of state-of-charge heterogeneity within a LiCoO₂ particle that evolves upon cycling at different rates," *ACS Energy Letters*, vol. 2, no. 5, pp. 1240–1245, May. 2017. I
- [7] Z. Jiang, J. Li, Y. Yang, L. Mu, C. Wei, X. Yu, P. Pianetta, K. Zhao, P. Cloetens, F. Lin *et al.*, "Machine-learning-revealed statistics of the particle-carbon/binder detachment in lithium-ion battery cathodes," *Nature Communications*, vol. 11, no. 1, p. 2310, 2020. I
- [8] G. Qian, J. Zhang, S.-Q. Chu, J. Li, K. Zhang, Q. Yuan, Z.-F. Ma, P. Pianetta, L. Li, K. Jung *et al.*, "Understanding the mesoscale degradation in nickel-rich cathode materials through machine-learning-revealed strain-redox decoupling," *ACS Energy Letters*, vol. 6, no. 2, pp. 687–693, Jan. 2021. I
- [9] G. J. Nelson, W. M. Harris, J. R. Izzo Jr, K. N. Grew, W. K. Chiu, Y. S. Chu, J. Yi, J. C. Andrews, Y. Liu, and P. Pianetta, "Three-dimensional mapping of nickel oxidation states using full field X-ray absorption near edge structure nanotomography," *Applied Physics Letters*, vol. 98, no. 17, p. 173109, Apr. 2011. I
- [10] M. Newville, "Fundamentals of XAFS," *Reviews in Mineralogy and Geochemistry*, vol. 78, no. 1, pp. 33–74, 2014. I, II-B
- [11] J. Prietzel, A. Botzaki, N. Tyufekchieva, M. Brettholle, J. Thieme, and W. Klysubun, "Sulfur speciation in soil by SK-edge XANES spectroscopy: comparison of spectral deconvolution and linear combination fitting," *Environmental Science & Technology*, vol. 45, no. 7, pp. 2878–2886, Mar. 2011. I
- [12] J. P. Gustafsson, S. Braun, J. M. Tuyishime, G. A. Adediran, R. Warrinnier, and D. Hesterberg, "A probabilistic approach to phosphorus speciation of soils using P K-edge XANES spectroscopy with linear combination fitting," *Soil Systems*, vol. 4, no. 2, p. 26, Apr. 2020.
- [13] D. Hesterberg, I. McNulty, and J. Thieme, "Speciation of soil phosphorus assessed by XANES spectroscopy at different spatial scales," *Journal of Environmental Quality*, vol. 46, no. 6, pp. 1190–1197, Nov. 2017. I
- [14] J. Li, B. Chen, G. Zan, G. Qian, P. Pianetta, and Y. Liu, "Subspace modeling enabled high-sensitivity X-ray chemical imaging," in *ICASSP 2023 - 2023 IEEE International Conference on Acoustics, Speech and Signal Processing (ICASSP)*, 2023, pp. 1–5. I, V-D
- [15] B. A. Anzures, S. W. Parman, R. E. Milliken, A. Lanzirrotti, and M. Newville, "XANES spectroscopy of sulfides stable under reducing conditions," *American Mineralogist: Journal of Earth and Planetary Materials*, vol. 105, no. 3, pp. 375–381, 2020. I
- [16] N. Keshava and J. F. Mustard, "Spectral unmixing," *IEEE Signal Processing Magazine*, vol. 19, no. 1, pp. 44–57, Jan. 2002. I, II-B
- [17] W.-K. Ma, J. M. Bioucas-Dias, T.-H. Chan, N. Gillis, P. Gader, A. J. Plaza, A. Ambikapathi, and C.-Y. Chi, "A signal processing perspective on hyperspectral unmixing: Insights from remote sensing," *IEEE Signal Processing Magazine*, vol. 31, no. 1, pp. 67–81, Jan. 2013. I
- [18] H. Li, R. Feng, L. Wang, Y. Zhong, and L. Zhang, "Superpixel-based reweighted low-rank and total variation sparse unmixing for hyperspectral remote sensing imagery," *IEEE Transactions on Geoscience and Remote Sensing*, vol. 59, no. 1, pp. 629–647, May 2020.

- [19] Z. Wang, J. Li, Y. Liu, F. Xie, and P. Li, "An adaptive surrogate-assisted endmember extraction framework based on intelligent optimization algorithms for hyperspectral remote sensing images," *Remote Sensing*, vol. 14, no. 4, p. 892, Feb. 2022. I
- [20] S. Tzoumas and V. Ntziachristos, "Spectral unmixing techniques for optoacoustic imaging of tissue pathophysiology," *Philosophical Transactions of the Royal Society A: Mathematical, Physical and Engineering Sciences*, vol. 375, no. 2107, p. 20170262, Oct. 2017. I
- [21] B. Ayhan, C. Kwan, and S. Vance, "On the use of a linear spectral unmixing technique for concentration estimation of APXS spectrum," *Journal of Multidisciplinary Engineering Science and Technology*, vol. 2, no. 9, pp. 2469–2474, Sep. 2015. I
- [22] T. YangDai and L. Zhang, "Spectral unmixing method for multi-pixel energy dispersive X-ray diffraction systems," *Applied Optics*, vol. 56, no. 4, pp. 907–915, 2017.
- [23] D. Rossouw, P. Burdet, F. de la Peña, C. Ducati, B. R. Knappett, A. E. Wheatley, and P. A. Midgley, "Multi-component signal unmixing from nanoheterostructures: Overcoming the traditional challenges of nanoscale x-ray analysis via machine learning," *Nano Letters*, vol. 15, no. 4, pp. 2716–2720, Mar. 2015. I
- [24] R. Heylen, M. Parente, and P. Gader, "A review of non-linear hyperspectral unmixing methods," *IEEE Journal of Selected Topics in Applied Earth Observations and Remote Sensing*, vol. 7, no. 6, pp. 1844–1868, May. 2014. I
- [25] J. M. Bioucas-Dias, A. Plaza, N. Dobigeon, M. Parente, Q. Du, P. Gader, and J. Chanussot, "Hyperspectral unmixing overview: Geometrical, statistical, and sparse regression-based approaches," *IEEE Journal of Selected Topics in Applied Earth Observations and Remote Sensing*, vol. 5, no. 2, pp. 354–379, Apr. 2012. I
- [26] L. Drumetz, M.-A. Veganzones, S. Henrot, R. Phlypo, J. Chanussot, and C. Jutten, "Blind hyperspectral unmixing using an extended linear mixing model to address spectral variability," *IEEE Transactions on Image Processing*, vol. 25, no. 8, pp. 3890–3905, Jun. 2016. I, II-B
- [27] D. Hong, N. Yokoya, J. Chanussot, and X. X. Zhu, "An augmented linear mixing model to address spectral variability for hyperspectral unmixing," *IEEE Transactions on Image Processing*, vol. 28, no. 4, pp. 1923–1938, Nov. 2018.
- [28] R. A. Borsoi, T. Imbiriba, J. C. M. Bermudez, C. Richard, J. Chanussot, L. Drumetz, J.-Y. Tourneret, A. Zare, and C. Jutten, "Spectral variability in hyperspectral data unmixing: A comprehensive review," *IEEE Geoscience and Remote Sensing Magazine*, vol. 9, no. 4, pp. 223–270, May. 2021.
- [29] L. Drumetz, J. Chanussot, C. Jutten, W.-K. Ma, and A. Iwasaki, "Spectral variability aware blind hyperspectral image unmixing based on convex geometry," *IEEE Transactions on Image Processing*, vol. 29, pp. 4568–4582, Feb. 2020.
- [30] S. G. Azar, S. Meshgini, S. Beheshti, and T. Y. Rezaii, "Linear mixing model with scaled bundle dictionary for hyperspectral unmixing with spectral variability," *Signal Processing*, vol. 188, p. 108214, Nov. 2021. I
- [31] M.-D. Iordache, J. M. Bioucas-Dias, and A. Plaza, "Total variation spatial regularization for sparse hyperspectral unmixing," *IEEE Transactions on Geoscience and Remote Sensing*, vol. 50, no. 11, pp. 4484–4502, May. 2012. I
- [32] I. A. Cruz-Guerrero, D. U. Campos-Delgado, and A. R. Mejía-Rodríguez, "Extended blind endmember and abundance estimation with spatial total variation for hyperspectral imaging," in *2021 43rd Annual International Conference of the IEEE Engineering in Medicine & Biology Society (EMBC)*, Nov. 2021, pp. 1957–1960. I
- [33] B. Lin, X. Tao, and J. Lu, "Hyperspectral image denoising via matrix factorization and deep prior regularization," *IEEE Transactions on Image Processing*, vol. 29, pp. 565–578, Jul. 2019. I
- [34] D. Gong, Z. Zhang, Q. Shi, A. van den Hengel, C. Shen, and Y. Zhang, "Learning deep gradient descent optimization for image deconvolution," *IEEE Transactions on Neural Networks and Learning Systems*, vol. 31, no. 12, pp. 5468–5482, Feb. 2020.
- [35] X. Wang, J. Chen, C. Richard, and D. Brie, "Learning spectral-spatial prior via 3DDNCNN for hyperspectral image deconvolution," in *ICASSP 2020-2020 IEEE International Conference on Acoustics, Speech and Signal Processing (ICASSP)*, Apr. 2020, pp. 2403–2407.
- [36] M. Zhao, X. Wang, J. Chen, and W. Chen, "A plug-and-play priors framework for hyperspectral unmixing," *IEEE Transactions on Geoscience and Remote Sensing*, vol. 60, pp. 1–13, Jan. 2021.
- [37] J. Chen, M. Zhao, X. Wang, C. Richard, and S. Rahardja, "Integration of physics-based and data-driven models for hyperspectral image unmixing: A summary of current methods," *IEEE Signal Processing Magazine*, vol. 40, no. 2, pp. 61–74, Feb. 2023. I
- [38] J. C. Andrews, E. Almeida, M. C. van der Meulen, J. S. Alwood, C. Lee, Y. Liu, J. Chen, F. Meirer, M. Feser, J. Gelb *et al.*, "Nanoscale X-ray microscopic imaging of mammalian mineralized tissue," *Microscopy and Microanalysis*, vol. 16, no. 3, pp. 327–336, 2010. II-A
- [39] Y. Liu, J. C. Andrews, J. Wang, F. Meirer, P. Zhu, Z. Wu, and P. Pianetta, "Phase retrieval using polychromatic illumination for transmission X-ray microscopy," *Optics Express*, vol. 19, no. 2, pp. 540–545, 2011. II-A
- [40] D. C. Heinz *et al.*, "Fully constrained least squares linear spectral mixture analysis method for material quantification in hyperspectral imagery," *IEEE Transactions on Geoscience and Remote Sensing*, vol. 39, no. 3, pp. 529–545, 2001. II-B
- [41] W. Meiniel, J.-C. Olivo-Marin, and E. D. Angelini, "Denoising of microscopy images: a review of the state-of-the-art, and a new sparsity-based method," *IEEE Transactions on Image Processing*, vol. 27, no. 8, pp. 3842–3856, 2018. III-B
- [42] J. Peng, W. Sun, H.-C. Li, W. Li, X. Meng, C. Ge, and

- Q. Du, "Low-rank and sparse representation for hyperspectral image processing: A review," *IEEE Geoscience and Remote Sensing Magazine*, vol. 10, no. 1, pp. 10–43, 2021. III-B
- [43] K. Dabov, A. Foi, V. Katkovnik, and K. Egiazarian, "Image denoising by sparse 3-d transform-domain collaborative filtering," *IEEE Transactions on Image Processing*, vol. 16, no. 8, pp. 2080–2095, 2007. III-C, V, V-B
- [44] K. Zhang, W. Zuo, Y. Chen, D. Meng, and L. Zhang, "Beyond a gaussian denoiser: Residual learning of deep cnn for image denoising," *IEEE Transactions on Image Processing*, vol. 26, no. 7, pp. 3142–3155, 2017. III-C, V, V-B
- [45] J. M. Nascimento and J. M. Dias, "Vertex component analysis: A fast algorithm to unmix hyperspectral data," *IEEE Transactions on Geoscience and Remote Sensing*, vol. 43, no. 4, pp. 898–910, Apr. 2005. 1, V-D
- [46] Z. Wen, C. Yang, X. Liu, and S. Marchesini, "Alternating direction methods for classical and ptychographic phase retrieval," *Inverse Problems*, vol. 28, no. 11, p. 115010, Oct. 2012. IV, 2
- [47] H. Chang, Y. Lou, M. K. Ng, and T. Zeng, "Phase retrieval from incomplete magnitude information via total variation regularization," *SIAM Journal on Scientific Computing*, vol. 38, no. 6, pp. A3672–A3695, Jan. 2016.
- [48] K. Bui and Z. Di, "A stochastic admm algorithm for large-scale ptychography with weighted difference of anisotropic and isotropic total variation," *arXiv preprint arXiv:2301.02386*, 2023. 2